Available online at www.sciencedirect.com
SCIENCE DIRECT®
ELSEVIER
Icarus 175 (2005) 1–14
ICARUS
www.elsevier.com/locate/icarus

Sulfur chemistry with time-varying oxygen abundance during Solar System formation

Matthew A. Pasek [a,*], John A. Milsom [b], Fred J. Ciesla [c], Dante S. Lauretta [a], Christopher M. Sharp [d], Jonathan I. Lunine [a]

[a] *Lunar and Planetary Laboratory, The University of Arizona, 1629 E University Blvd., Tucson, AZ 85721, USA*
[b] *Department of Physics, The University of Arizona, 1118 E Fourth Street, Tucson, AZ 85721, USA*
[c] *NASA Ames Research Center, MS 245-3, Moffet Field, CA 94035, USA*
[d] *Steward Observatory, University of Arizona, 933 N Cherry Ave, Tucson, AZ 85721, USA*

Received 24 October 2003; revised 8 October 2004

Available online 25 February 2005

Abstract

Chemical models of solar nebula chemistry are presented which show the influence of progressive water depletion from the inner solar nebula. The main focus of this work is the equilibrium distribution of S resulting from this process. Under canonical solar nebula conditions, H_2S is the dominant S-bearing species in the gas phase and troilite (FeS) is the primary reservoir for S after condensation. As water vapor diffuses out to its condensation front, the equilibrium distribution of S changes significantly. With the removal of water vapor, SiS becomes the most abundant S-bearing gas and MgS and CaS compete with FeS as the main sulfide reservoir. These results allow us to argue that some of the minerals in the enstatite chondrites formed through the heterogeneities associated with the nebular ice condensation front, and that the sulfur abundance in Jupiter reflects a depletion in H_2S that is the result of inner nebula sulfur chemistry under varying oxygen abundance.

Keywords: Solar nebula; Meteorites; Cosmochemistry; Jupiter

1. Introduction

The importance of water as a condensable and chemically active species in protoplanetary disks has long been emphasized in planetary literature. The time-varying location at which water is saturated in a formal thermodynamic sense—"the snow line"—can be considered the dividing line not only between the inner and outer Solar System but also between the solar nebula of the meteoriticist and that of the planetary astronomer (Lunine et al., 2000). Understanding the coupling between rocky and icy solids has been difficult for several reasons. Primitive meteorites do not contain water ice or other more volatile species. Our knowledge of the presence of meteoritic water is limited to the identification of mineralogic changes in primitive meteorites due to aqueous alteration from water resulting from the melting of icy material on a meteorite's parent body. In addition, astronomical observations of comets have not simultaneously tracked abundances of both silicates and ices. Here we attempt to bridge some of these gaps by investigating the influence of diffusive water vapor redistribution to the snow line in the early Solar System on the major-element chemistry of the inner solar nebula.

This work has important implications for the composition of planetary bodies on both sides of the snow line. The Galileo probe measurements of elemental abundances in Jupiter include sulfur as well as noble gases, carbon, nitrogen, and oxygen, which, unfortunately, is drastically affected by meteorology (Atreya et al., 2003). These elemental abundances constrain the mechanisms by which Jupiter acquired its inventory of heavy elements ($Z > 2$), which are well above solar abundance inside all the giant planets. To un-

* Corresponding author. Fax: +1-520-621-4933.
E-mail address: mpasek@lpl.arizona.edu (M.A. Pasek).

0019-1035/$ – see front matter
doi:10.1016/j.icarus.2004.10.012

derstand how these abundances relate to the composition of planetesimals that fed Jupiter requires considering processes in both the inner and outer Solar System and considering the interaction between dynamics and chemistry. Indeed, as we show in the present paper, oxygen (water) and sulfur-bearing compounds cannot be considered apart from each other, because the chemistry of sulfur and hence the abundance of its principal volatile molecular form, hydrogen sulfide, is greatly affected by the oxygen abundance. Furthermore, observations of circumstellar disks suggest that sulfur is depleted in the gas phase relative to cosmic abundance. That is, H_2S is not the only or even the primary sulfur-bearing species in these disks. These observations suggest that refractory phases contain much of the sulfur in these environments (Dutrey et al., 1997).

The present paper quantifies, in more detail than previous work, the chemistry of sulfur-bearing phases in a solar-abundance protoplanetary disk model. However, it goes a step further by examining the sulfur chemistry under various oxygen fugacities in the inner solar nebula (within 5 AU), which result from the time-variable water vapor abundance inward of a cold-trapping condensation front in the disk (Morfill and Volk, 1984). Water is moved from sunward of the snowline out to the condensation front as a result of diffusion driven primarily by radial concentration gradients. Using a simple model of nebular dynamics, we show how the oxygen-dependent chemistry and laboratory based reaction kinetics can explain a depletion of hydrogen sulfide in the disk. Such a depletion may in turn be reflected in the elemental abundance pattern constrained in Jupiter by the Galileo Probe.

Section 2 of the paper describes the nebular model we use to determine the temperature and pressure with respect to time, while Section 3 details the chemical equilibrium codes used. In Section 4 we consider the coupled effects of the sulfur chemistry, the reaction kinetics, and the changing oxygen abundance due to nebular water transport and condensation on the abundances of the primary sulfur-bearing species. The results are relevant to meteorites, circumstellar disks, and the elemental abundances in Jupiter, as discussed in the final section.

2. Nebular model

To properly evaluate the changing chemistry in the disk, we need a time-dependent model of the solar nebula which gives us the pressure and temperature at each radius as a function of time. In this paper, we use the two-dimensional steady state disk solutions of Huré (2000) as they have been applied by Hersant et al. (2001). Other models of the solar nebula produce qualitatively similar results (Cassen, 2001). These axisymmetric disk solutions use an α viscosity (see, e.g., Shakura and Sunyaev, 1973) and they include the effects of turbulent pressure, convection, and self-gravity. To use these steady state solutions, we must know the accretion rate onto the Sun as a function of time. In these calculations, the accretion rate onto the Sun is described by a power law (see Makalkin and Dorofeyeva, 1991)

$$\dot{M}(t) = \dot{M}_0(1 + t/\tau)^{-s}.$$

In this equation, t is the time after the Sun is almost completely formed. Hence, this equation describes the quiescent period of the nebula in which the nebula cools as time passes and the accretion rate onto the Sun continuously drops. $\dot{M}_0$ is the accretion rate at $t = 0$ and τ is the accretion timescale,

$$\tau = \frac{R_{D0}^2}{3\nu_{D0}}$$

where R_{D0} is the initial outer radius of the disk and ν_{D0} is the turbulent viscosity at R_{D0} at $t = 0$. As in Drouart et al. (1999), we use $s = 1.5$ for the power law exponent. This power law decay of the accretion rate is consistent with observations of T Tauri stars (see Hartmann et al., 1998).

Note that while the disk solutions of Huré (2000) are infinite in extent, these disks must be finite so they are cut off at R_{D0} at $t = 0$. As time passes, the disk expands due to the redistribution of angular momentum in the viscous disk so the outer radius of the disk increases with time.

In this scenario, $\dot{M}_0$, R_{D0}, and α are all variable parameters. We follow the work of Hersant et al. (2001) which constrains these parameters using four criteria. First, the total disk mass must be large enough to form all the planets but $\leqslant 0.3 M_\odot$ so that the disk is not gravitationally unstable (Shu et al., 1990). Second, angular momentum must have been transported outward to where Neptune would form in 2.5×10^5 years so that icy and rocky grains could decouple from the gas and ultimately form the core of Neptune. Third, the temperatures inside 3 AU must be $\geqslant 1000$ K at early times in the nebula evolution in order to explain the crystalline silicate distributions in meteorites and comets (see Bockelée-Morvan et al., 2002). Lastly, the nebula model must yield deuterium enrichments in the planets and meteorites consistent with observations. Hersant et al. (2001) find that there exists a range of acceptable disk solutions which satisfy these criteria. Specifically, they conclude that $0.006 \leqslant \alpha \leqslant 0.04$, 12.8 AU $\leqslant R_{D0} \leqslant 39$ AU and $2.2 \times 10^{-6} M_\odot/\text{year} \leqslant \dot{M}_0 \leqslant 1 \times 10^{-5} M_\odot/\text{year}$.

From these acceptable models, they define a "nominal" model which has $\dot{M}_0 = 5 \times 10^{-6} M_\odot/\text{year}$, the dimensionless parameter $\alpha = 0.009$ and $R_{D0} = 17$ AU. This model yields an initial disk mass of $0.24 M_\odot$. In this paper, we focus our chemical calculations on this "nominal" model. The pressures and temperatures needed as input to our chemical equilibrium codes (see Section 3) are the midplane pressures and temperatures in this "nominal" time-dependent two-dimensional disk model. In Fig. 1, we plot the midplane temperature in this nominal model versus radius for four different times. While focusing on the nominal model, we also investigated the sulfur chemistry using other models which satisfied their four criteria. Specifically, we also used the "warm" and "cold" models defined in Table 2 of Hersant et

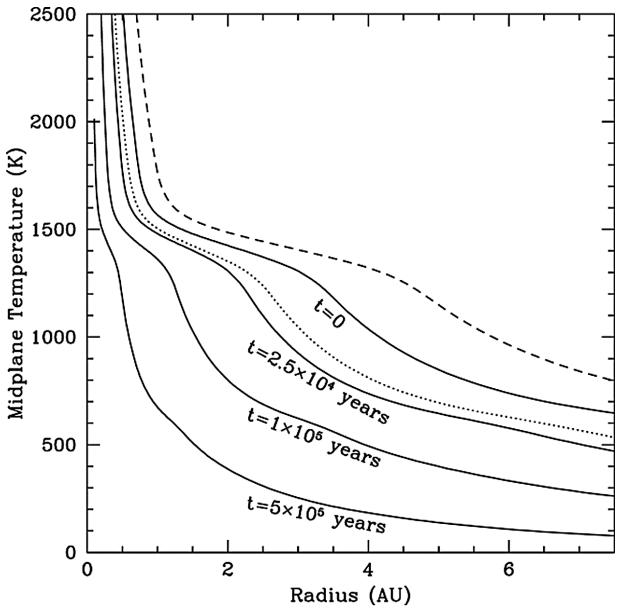

Fig. 1. Graph showing the time dependence of temperature versus radial distance in the "nominal" solar nebula model from Hersant et al. (2001). The dashed and dotted curves represent the time zero distribution in their "warm" and "cold" models for comparison.

al. (2001). These models are, on average, warmer (or colder) than the nominal model throughout the disk at a fixed time. The difference between the warm, cold and nominal models is illustrated in Fig. 1 for time zero. Additional plots of the structure of these nebulae can be found in Hersant et al. (2001).

3. Description of chemical equilibrium codes

We used two different chemical equilibrium codes to determine the abundances of sulfur species in the solar nebula. For both codes we use a pressure–temperature profile defined from the nebular model described in Section 2. The use of two distinct chemical equilibrium codes with slightly different thermodynamic databases provides an internal check on the results. We now describe each of the codes in detail.

We use a modified version of the SOLGASMIX code (Bessman, 1977) which is described in Sharp and Huebner (1990, 1993) and Burrows and Sharp (1999). The original version of SOLGASMIX was obtained from the Los Alamos National Laboratory in the mid 1980s. It was written for a maximum of ten chemical elements and a limited number (less than about 50) of different chemical species. In addition to gaseous species, it has the capability of handling condensed phases and solutions and it was originally intended for chemical engineering calculations. The abundances of all the gaseous and condensed phase species were calculated by minimizing the total Gibbs free energy of the system. However, the maximum number of species the code could handle was far too small for realistic astrophysical calculations. Among a considerable number of enhancements made to the code over a period of time, the limit of the maximum number of elements was increased to 40 and the total number of species was increased to 1000. For calculations described here, as in Burrows and Sharp (1999), we use only gas phase and solid species with no solid solutions.

SOLGASMIX uses the White et al. (1958) algorithm in which the total dimensionless Gibbs free energy of the system is minimized using the method of Langrange undetermined multipliers (Eriksson and Rosen, 1973). The calculations are subject to the constraint that the total number of atoms of each element is conserved. The activity of a gas phase species is its partial pressures in atmospheres, and the activity of a condensate is unity (for calculations and the method of approach, see (Sharp and Huebner, 1990)).

The chemical database for this code has been updated for this work to account for previous errors and to include critical sulfur and oxygen species and compounds that become important at increased C/O ratios. Specifically, we include updated data for gaseous PH, PH_3, PN, and solid $Mg_3(PO_4)_2$ from Lodders (1999). This corrects for errors in the JANAF tables (Chase, 1982, 1998). We also correct for an error in the JANAF table for gaseous HS using data from Barin (1995). We include the following sulfur species which were not previously in the database: gaseous Al_2S and AlS_2 (Gurvich et al., 1994), solid $FeCr_2S_4$ (Petaev et al., 1986), solid $CaSO_4$ and $(NH_4)_2SO_4$ (Barin, 1995), solid and gaseous TiS (Barin, 1995) and solid CrS (Barin, 1995). We also include data from Barin (1995) for the solids Cr, CrN, Cr_2N, Cr_2O_3, TiO_2, Ti_2O_3, Ti_3O_5, Ti_4O_7, Fe_3C, Al_2O_3, CaO, $CaAl_2Si_2O_8$, $CaAl_4O_7$, $CaAl_2O_4$, $CaTiO_3$, $Ca_4Ti_3O_{10}$, $Ca_3Ti_3O_7$, $FeSiO_3$, $MgTiO_3$, Mg_2TiO_4, $MgTi_2O_5$, $MnSiO_3$, Mn_2SiO_4, $FeCr_2O_4$, and for the gas phase species CaH, TiO, CrO, CrO_2, and CrO_3. Some of these species were already in the database but were updated for consistency. Additionally, we have included solid Fe_3P from Knacke et al. (1991) and solid $CaAl_{12}O_{19}$ from Hallstedt (1990). Lastly, we have included gaseous CrH from Burrows (private communication), gaseous FeH based on spectroscopic data in Dulick et al. (2003), gaseous TiH from Bernath (private communication) and gaseous MgH based on spectroscopic data in Weck et al. (2003). As no thermodynamic data were readily available for these four metal hydrides, the thermodynamic data are calculated from the dissociation potentials and partition functions, which are in turn calculated from asymptotic formulae for the vibrational and rotational constants of each electronic state (Kassel, 1933a, 1933b).

We also performed calculations using the equilibrium module in the HSC Chemistry (v5.1) software package (Outokumpu Research Oy, Finland). This code uses the GIBBS energy minimization equilibrium solver (White et al., 1958). For the purposes of these calculations, all solutions were assumed to be ideal (i.e., $\gamma = 1$). The thermodynamic database provided with this code is frequently updated. Most of the species considered in the SOLGASMIX chemical code were also considered in the HSC5 code, although with a few no-

Table 1
Solar abundances used, taken from Grevesse and Sauval (1998) and Prieto et al. (2001, 2002)

Element	Abundance
H	9.10×10^{-1}
He	8.89×10^{-2}
O	4.46×10^{-4}
C	2.23×10^{-4}
Ne	1.09×10^{-4}
N	7.57×10^{-5}
Mg	3.46×10^{-5}
Si	3.30×10^{-5}
Fe	2.88×10^{-5}
S	1.44×10^{-5}
Al	2.81×10^{-6}
Ar	2.29×10^{-6}
Ca	2.04×10^{-6}
Na	1.90×10^{-6}
Ni	1.62×10^{-6}
Cr	4.46×10^{-7}
P	3.30×10^{-7}
Mn	3.08×10^{-7}
Cl	1.73×10^{-7}
K	1.23×10^{-7}
Ti	7.93×10^{-8}
Co	7.40×10^{-8}
F	2.75×10^{-8}

The values are normalized to 1 mole total.

table distinctions. Ar gas and Mn- and Co-bearing species were omitted from the calculations, as their inclusion resulted in instability with the code, mainly due to limitations in the code on the number of total elements allowed for calculation. Fortunately, these elements are in low enough abundance that their exclusion does not affect sulfur chemistry. However, fluorine-bearing gases and condensates were included, unlike in the SOLGASMIX code. The thermodynamic data for the species shown in Appendices A.1 and A.2 are available in the thermodynamic database of the code, with the exception of Fe_3P, the data for which are found in Zaitsev et al. (1995) and Fe_3C, the data for which are in Barin (1995).

The elemental abundances from Grevesse and Sauval (1998) were used in these calculations, with several exceptions. Corrections to Grevesse and Sauval's (1998) values for oxygen and carbon come from Prieto et al. (2001, 2002). Table 1 lists the standard solar elemental abundances used in the calculations. Appendices A.1 and A.2 list the chemical species used in each code.

All the calculations described in this paper have been performed using both codes. In all cases, the results from both codes are similar. To illustrate the similarity of the codes, we present the condensation sequence at a pressure of 10^{-6} bars (Table 2) with solar abundances using both codes and also compare the results to Yoneda and Grossman (1995). In particular, the species Al_2O_3, Mg_2SiO_4, Fe, $MgSiO_3$, FeS, and the feldspars ($NaAlSi_3O_8$, and $KAlSi_3O_8$) are all in relative agreement. Most of the differences between the two codes

Table 2
Temperatures of appearance and disappearance at 10^{-6} bars from the two codes used and Yoneda and Grossman (1995- sixth and seventh columns)

Compound	SOLGASMIX		HSC		Y and G 95	
	In	Out	In	Out	In	Out
Al_2O_3	1542	1484	1535	1501	1571	1481
$CaAl_{12}O_{19}$	1496	1251	1501	1292	1485	1292
$CaTiO_3$	1447	1423	1447	1419	1471	1257
$Ca_2(Mg,Al)(Si,Al)_2O_7$[a]			1430	1251	1405	1264
$Ca_4Ti_3O_{10}$	1423	1250	1419	1235	NI	NI
$Ca_2Al_2SiO_7$[a]	1340	1308				
Al_2O_3	1308	1251	1300	1261	1292	1286
$MgAl_2O_4$					1286	1266
$CaAl_2Si_2O_8$	1253	1237	1261		1268	1250
$CaTiO_3$	1250	1216	1283	1221		
$Ca_2MgSi_2O_7$[a]	1245	1242				
$CaMgSi_2O_6$	1243		1236		1257	
$MgAl_2O_4$	1239	1194	1228		1252	1227
Mg_2SiO_4	1230		1228		1246	
Ti_4O_7	1216		1221			
Fe	1201		1201		1214	
$CaAl_2Si_2O_8$	1197	1054			1234	
$MgSiO_3$	1179		1208		1195	
Fe_3P	1114	632	1153	723	NI	NI
$MgAl_2O_4$	1054				1161	
$KAlSi_3O_8$	815		805		NI	NI
$NaAlSi_3O_8$	810		832			
FeS	691		689			
$Ca_3P_2O_8$	632		723		NI	NI

All calculations use solar abundances and Yoneda and Grossman did not extend their calculations below 1000 K. Species denoted by NI were not included in Yoneda and Grossman.
[a] In our calculations using SOLGASMIX we divided the melilite solid solution species into two different end members, whereas our HSC calculations and Yoneda and Grossman did not.

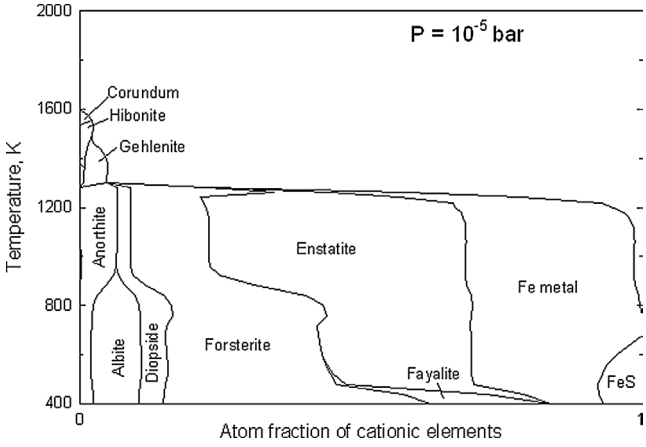

Fig. 2. Equilibium condensation sequence for a system at 10^{-5} bar and solar abundance. Legends follow Wood and Hashimoto (1993).

are due to solid solution assumptions. The condensation sequence generated by the HSC code at 10^{-5} bar (Fig. 2) is in agreement with prior calculations (Wood and Hashimoto, 1993). The graphical results we present in Fig. 4 are those obtained using the SOLGASMIX code.

4. Sulfur chemistry results

4.1. Chemical equilibrium calculations

We use the time-dependent disk model and the equilibrium codes described in Section 3 to determine the locations of condensation fronts in the solar nebula. A set of calculations was performed to determine equilibrium chemistry at the beginning of the quiescent stage of nebular evolution (time zero), when the inner regions of the disk were quite hot. We restricted our calculation to regions for which $T < 2500$ K, where ionization effects are negligible. At time zero, this temperature occurs at a distance of 1 AU. The condensation fronts migrate inward as time passes and the disk cools (Fig. 3). Troilite and H_2S are the major sulfur-bearing solid and gas species, respectively, and HS, SiS, S, PS, S_2, and AlS are additional minor gas species at all stages of disk evolution with solar compositions. The ice condensation front is located at 5 AU after $\sim 4.4 \times 10^5$ years of disk evolution. The troilite condensation front is always ahead of that for water ice and reaches the inner regions of the nebula ($r < 5$ AU) in less than 10^5 years.

Recent work suggests that large variations in major element chemistry may have occurred in the solar nebula. In particular, Cyr et al. (1998, 1999) suggest that the oxygen abundance in the inner nebula was depleted relative to solar as a result of diffusive water vapor redistribution, which is thought to overwhelm the inward drift of ice particles. The depletion of water vapor results in reduced oxygen abundances in the inner region of the nebula (dashed curves in Fig. 3) and affects the locations of these two condensation fronts. Gases other than water (like CO_2, CH_4, and CO) do not diffuse outwards as a result of the removal of water vapor, thus the amount of carbon in the system remains constant relative to a depletion in oxygen. These gases (CO, CH_4, and CO_2) condense at temperatures significantly lower than the water condensation point (i.e., their "sinks" occur further out in the radius of the nebula), thus diffusion is less significant because of lower concentration and temperature gradients. It is true that a minor pressure gradient will result from the removal of H_2O vapor; however, the abundance of H_2 and He gases remain unaffected by water vapor redistribution and it is these gases that determine the total pressure of the nebula. Condensation of graphite may hypothetically occur as a result of the depletion of oxygen. However, our code assumes that any graphite that forms is in contact with the other equilibrium phases and is thus not removed from the system (i.e., in full equilibrium). In addition, the kinetics for the formation of graphite depend largely on the gaseous abundance of long chains of carbon (Salpeter, 1974) and our equilibrium calculations and those of Larimer and Bartholomay (1979) do not suggest the abundance of these chemicals. These molecules are mainly a result of disequilibrium processes, thus the majority of C remains in the gaseous phase as CH_4. As a result, the C/O ratio resulting from the depletion of water remains dependent only on the amount of water removed from the system.

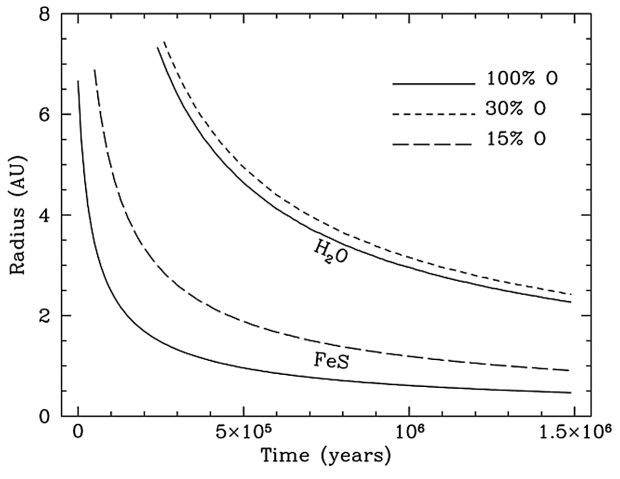

Fig. 3. The locations of condensation fronts of troilite and water ice with respect to time. Note that these condensation fronts use the condensation temperature at the start of condensation, not the 50% condensation temperature. As the early solar nebula cooled, the condensation fronts of both sulfur and water moved inwards. The locations of both fronts are dependent upon oxygen fugacity, as shown by the separate lines drawn for lower oxygen fugacities. With an oxygen removal greater than 30%, water ceases to appear in our calculations, and with an oxygen removal greater than 15%, troilite no longer condenses. Here we have shown the lower limits of the stability of these compounds.

Our equilibrium calculations indicate that the condensation temperature for troilite is 690 K for oxygen abundances above 25% of the solar oxygen abundance (or equivalently C/O = 2). The equilibrium constant for the troilite formation reaction,

$$\mathrm{Fe} + \mathrm{H_2S\ (g)} \rightarrow \mathrm{FeS} + \mathrm{H_2\ (g)},$$

is pressure independent since the number of moles of gas is the same on each side of the reaction. For lower oxygen abundances (or higher C/O ratios), the troilite condensation temperature drops because other sulfur species become more stable (specifically solid MgS). Figure 3 illustrates the effects of extreme oxygen depletion (15% solar O abundance or equivalently C/O = 3.33) on the location of troilite condensation front. In this case, the troilite condensation temperature varies between 400 K (at a pressure of 5.6×10^{-7} bars) at early times to 417 K (at a pressure of 2.7×10^{-6} bars) at later times. For oxygen abundances of $<$ 12.5–15% in a solar-composition gas (C/O $\gtrsim$ 3.5–4), troilite is not present in an equilibrium mixture and MgS is the primary S-bearing solid.

The condensation temperature of water changes only slightly when the oxygen abundance is reduced. Under solar abundance conditions, the condensation temperature of ice varies between 151 and 155 K. For cases where the O abundance is 30% solar (C/O = 1.66) as in Fig. 3, the ice condensation temperature varies from 143 to 146 K. If the oxygen abundance is $\lesssim$ 25–30% solar (C/O $\gtrsim$ 1.66–2), H_2O solid does not appear in an equilibrium mixture since all the oxygen is in the magnesium silicates ($MgSiO_3$ and

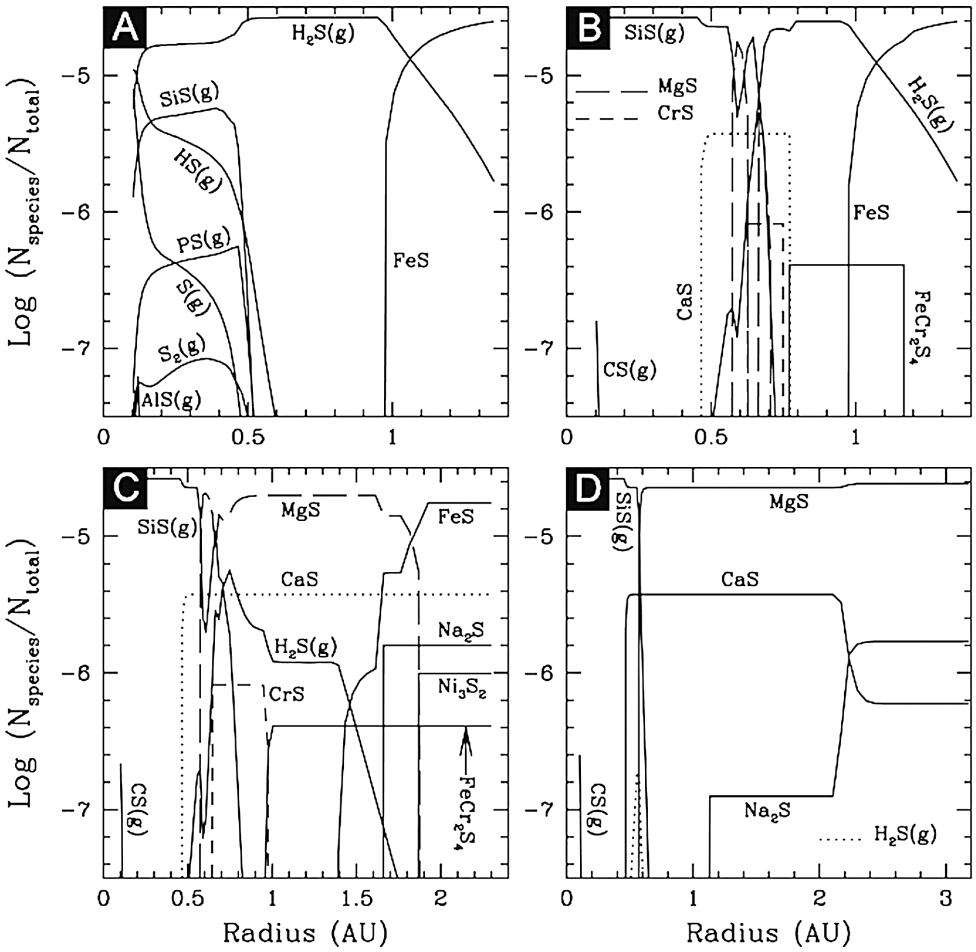

Fig. 4. Graph showing the dependence of major sulfur-bearing species on relative oxygen abundance at a time of 5×10^5 years. As oxygen is removed from the system (B, C, and D), SiS and MgS become the dominant S-bearing gas and solid, respectively. For reference, the temperatures in each panel at 0.5, 1.0, 1.5, 2.0, 2.5, and 3.0 AU are respectively 1180, 672, 509, 387, 308, and 253 K. (A) 100% of the initial oxygen. (B) 33% of the initial oxygen. (C) 20% of the initial oxygen. (D) 10% of the initial oxygen.

Mg_2SiO_4). These calculations show that the temperature of ice condensation is relatively insensitive to the bulk O abundance.

The overall effect of depleted water on sulfur chemistry is illustrated in Fig. 4, in which we show the distribution of sulfur species in the nebula at $t = 5 \times 10^5$ years for a range of radii and for four different oxygen fugacities. The vertical axis is effectively the log of the mixing ratio of that species since N_{total} represents the total number of gas particles present at that pressure and temperature. We assume that the pressure and temperature are related by the ideal gas law. All species in the figure are solid phase species unless they are followed by a (g). The innermost radius for which we plot data in Fig. 4 is 0.1 AU, which is the innermost data point in the Hersant et al. (2001) profile.

H_2S (g) is the dominant sulfur species throughout most of the nebula when the oxygen abundance is solar (Fig. 4A). At 0.98 AU (where $T = 690$ K), troilite begins condensing. At larger radii all the sulfur is converted to troilite. Iron is twice as abundant as sulfur so it is theoretically possible for 100% of the sulfur to be converted into troilite. However there are dynamical issues that must also be considered. It is possible that the diffusion of H_2S gas will alter the local abundance of sulfur. It is also possible that the reaction to produce troilite will occur too slowly to convert all the sulfur in H_2S (g) into troilite in the lifetime of the nebula. These issues will be explored in more detail in Sections 4.2 and 4.3. We emphasize here that these graphs display the equilibrium abundances ignoring all dynamical effects.

Our graphs are limited by certain features of our computer codes, especially at lower temperatures. The presence of many stable solids at lower temperatures makes finding a solution difficult. Under these conditions, the SOLGASMIX code is unable to determine the equilibrium mixture for temperatures below 559 K ($r > 1.35$ AU). Reducing the total number of species resolves some of these problems. The HSC code is able to find solutions at temperatures down to ~ 100 K.

The equilibrium distribution of sulfur is significantly affected by progressive depletion of H_2O (g). When the inner nebula is depleted down to 33% of the original solar O abundance (C/O = 1.5), a significant change in S chem-

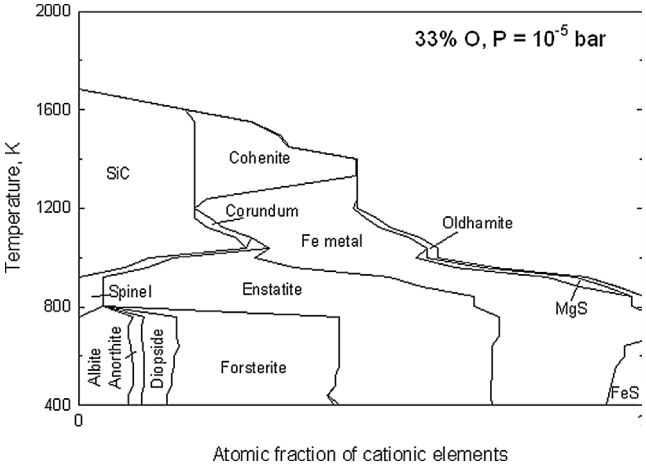

Fig. 5. Equilibrium condensation sequence for a system at 10^{-5} bar and with 33% of starting O (as per Fig. 4B). Legends follow Wood and Hashimoto (1993).

istry occurs (Fig. 4B). At temperatures above 920 K, SiS replaces H_2S as the primary sulfur-bearing gas species. Between 650 and 920 K, H_2S is the dominant sulfur gas species and the only other sulfur gas phase species present in significant abundance is CS. Below 650 K, troilite is the dominant sulfur-bearing species. However, many other condensed sulfurous species are also stable. Oldhamite (CaS) exists between 785 and 1272 K and contains a large proportion of the total Ca. Chromium and Mg are also chalcophilic under these conditions, forming $FeCr_2S_4$, CrS, and MgS. Under these conditions, MgS is abundant in a narrow temperature range (between 900 and 1100 K) and becomes significantly more abundant as the oxygen abundance is reduced even further. As the abundance of O decreases, Mg and Ca are both forced to enter sulfide phases as there is not enough O available to form silicates, and this is a general trend we observe in our models.

Under these conditions the total mineralogy is significantly different. Reduced minerals such as cohenite and silicon carbide dominate at higher temperatures, replacing silicates. Clearly the equilibrium between enstatite and forsterite is affected, with enstatite always present below ~ 1000 K. The overall mineralogy is shown in Fig. 5.

The distribution of S changes even more dramatically when the O abundance is reduced to 20% solar (C/O = 2.5) (Fig. 4C). In Section 4.3 we will show that such conditions are unlikely for the solar nebula, but may be possible if water vapor continuously diffuses out to the condensation front and the resulting condensates do not migrate back inwards and increase the O abundance. Under these reducing conditions, solving for chemical equilibrium at low temperatures is easier since fewer solid oxides are stable. Thus, our calculations for these systems extend to larger radii (where $T \sim 336$ K). The intermediate temperature region is now dominated by MgS. Overall SiS (g), MgS and troilite are the primary S-bearing phases as the system cools from high to low temperatures. H_2S is a minor species in the gas phase. The troilite condensation front is at 1.4 AU, where $T \sim 547$ K. Troilite equals MgS in abundance at ~ 1.8 AU ($T \sim 420$ K). At this low temperature, troilite formation kinetics may be too sluggish to allow for significant troilite production.

Two additional solids, Na_2S and Ni_3S_2, are stable under these conditions (Fig. 4C). The stability of Ni_3S_2 is doubtful. The most abundant nickel-bearing sulfide in highly reduced meteorites is pentlandite [$(Fe,Ni)_9S_8$]. However, there are limited thermodynamic data for this phase and thus it is not considered in our calculations. The Ni_3S_2 phase is used as a proxy for pentlandite and its presence in our calculations indicates that a nickel sulfide mineral is likely to be stable and probably in solid solution with troilite. The solar abundances of sodium and nickel are both low enough that they play only a minor role in sulfur chemistry.

Troilite is not stable under the most reducing conditions that we studied, a nebula depleted to 10% solar O (C/O = 5, see Fig. 4D). The most abundant S-bearing gas under these conditions is SiS. MgS condenses at ~ 1000 K. CaS and Na_2S are also stable and together contain about 9% of the sulfur. Chromium condenses into the bulk metal and Cr_2N is stable at lower temperatures. Our equilibrium calculations suggest that the sulfides MgS, Na_2S, and CaS dominate at these low temperatures. These extremely reducing conditions cannot occur in the diffusive model we describe below in Section 4.3. This is due to the limitation that the removal of oxygen can only proceed to the point where all water is removed from the system. At a removal of about 80% of the total oxygen, the remainder of the oxygen is stored in silicate or solid oxide compounds. These compounds do not react with hydrogen gas to yield more water vapor, since the oxides and silicates are thermodynamically favored compared to water. The only case where this would be a realistic approximation is in the case of carbon stars, where the initial C/O ratio is 5 or so.

One of the most significant changes in the equilibrium distribution of S that results from H_2O depletion in the inner nebula is the transition from H_2S to SiS as the dominant S-bearing gas. It is worth examining this transition in more detail (Fig. 6). At 80% O, H_2S is more abundant than SiS in the high temperature regions. At 70% O, the abundance curves for H_2S and SiS cross twice and overall both have similar abundances in the region $r \lesssim 0.63$ AU ($T \gtrsim 950$ K). At 60% O, SiS is the more abundant species. Thus, 70% O effectively represents the transition between H_2S dominating at high temperatures and SiS dominating at high temperatures.

While the change from 80% O to 60% O dramatically changes the high-temperature chemistry, it has a negligible effect on the low-temperature chemistry. The stability fields of H_2S (g) and troilite are similar in all three cases. The major difference is the Cr distribution. Six percent of total S is in $FeCr_2S_4$ at O abundances of 70 and 60% of solar, resulting in 6% less troilite. At an O abundance of 60% solar MgS is stable over a small temperature interval.

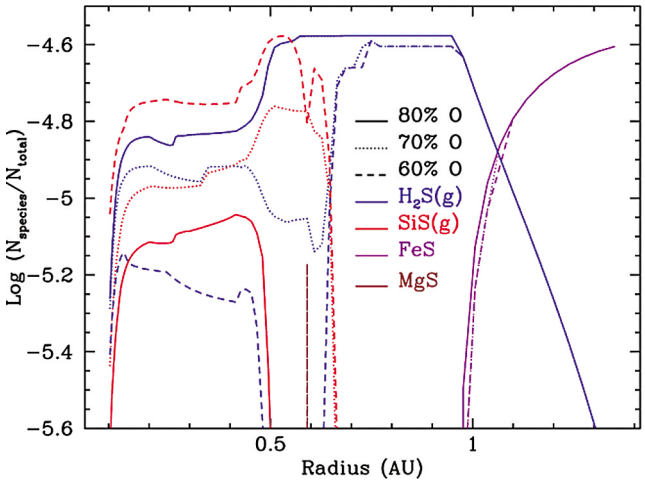

Fig. 6. Graph demonstrating the H_2S/SiS transition with changing oxygen abundance at a time of 5×10^5 years. At solar oxygen, H_2S is more abundant than SiS, but when the O abundance becomes less than 70% of solar, SiS becomes the major S-bearing gas species. The figure graphs the abundance of the most abundant species only (H_2S, SiS, troilite and MgS) for 80% O, 70% O and 60% O. Note that the vertical scale is different from that of Fig. 4.

The calculations described above are specific to the "nominal" model from Hersant et al. (2001). We also performed calculations using the "warm" and "cold" models defined in their paper and illustrated here in Fig. 1. The condensation fronts occur at larger radii and the gas phase species extend to larger radii in any warmer model (and vice versa for any colder model). However, the general appearance of the sulfur distribution (as a function of oxygen percentage) does not change. Thus, the results described above qualitatively describe the equilibrium sulfur chemistry for a range of nebular models.

Our equilibrium calculations do not account for reaction kinetics. One of the most important reactions is FeS formation from the reaction of H_2S gas with Fe metal. The gas–solid reaction kinetics are dependent on sulfur abundance, iron metal grain size, and temperature. We address the issue of kinetics in the following section.

4.2. Sulfide formation kinetics

Unlike H_2O, which condenses directly into the solid state, S is incorporated into solid material through the gas–solid reaction of iron with H_2S (g) to form troilite. As a result of this reaction pathway, it is necessary to consider the kinetics of this reaction to compare the timescales for sulfur condensation to the evolution timescales of a protoplanetary accretion disk. We have performed these calculations in the context of a slowly cooling nebula whose inner regions are continuously depleted in H_2O vapor as a result of diffusion out to the snow line. The reaction kinetics for sulfide formation have been measured in a series of experimental studies (Lauretta et al., 1996, 1997, 1998). We use the results of these studies to estimate the timescales for S condensation.

Reaction kinetics were measured in H_2S–H_2 gas mixtures containing 25–10,000 ppm H_2S. The solar abundance of S suggests that H_2S was present in the solar nebula at an abundance of 27 ppm (Lodders, 2003). Experiments were performed both with pure Fe metal (Lauretta et al., 1996) and with meteoritic alloys (Lauretta et al., 1997, 1998). These studies show that the rate of troilite formation varies as a function of temperature, H_2S and H_2 partial pressures, metal composition, and metal grain size. For small metal grains the rate-limiting step in the solar nebula was either the delivery of H_2S gas molecules to the metal surface or the dissociation of H_2S.

In the near-vacuum conditions of the solar nebula it is more likely that the supply of gas molecules to the metal surface is the rate-limiting step. This scenario can be modeled using the simple collision theory developed by Fegley (1988). The time to condense all S (t_{chem}) in seconds is:

$$t_{\text{chem}} = \frac{[H_2S]}{\left(\frac{2.635\times10^{25}\cdot P_{H_2S}}{(M_{H_2S}\cdot T)^{1/2}}\right)\cdot A_{\text{Fe}}\cdot\exp\left(\frac{-E_{\text{act,FeS}}}{RT}\right)}.$$

In this equation $[H_2S]$ is the abundance of H_2S (g) in mol cm^{-3}, P_{H_2S} is the partial pressure of H_2S in bars, M_{H_2S} is the molecular weight of H_2S in g mol^{-1}, T is the temperature in K, A_{Fe} is the surface area per unit volume of Fe metal grains in cm^2 cm^{-3} of the solar nebula, which varies as a function of average metal grain size, $E_{\text{act,FeS}}$ is the activation energy for troilite formation in Joules/mol, and R is the gas constant (8.314 J mol^{-1} K^{-1}). The constant 2.635×10^{25} has units of (g K mol)$^{1/2}$ cm^{-2} bar^{-1} s^{-1}. We use this equation to estimate the troilite formation timescales.

Experimental studies of Fe sulfurization in 100 ppm H_2S (g) displayed Arrhenius behavior and yielded an activation energy of 49 kJ mol^{-1} (Lauretta et al., 1996). Sulfurization of both pure Fe and meteoritic metal in 50 ppm H_2S did not display Arrhenius behavior (Lauretta et al., 1996, 1998). Instead, in both studies it was observed that the reaction rates at the lower temperatures ($T < 613$ K for pure Fe and $T < 558$ K for the meteoritic metal) were larger than those at the higher temperatures. As a result a value for the activation energy from these experiments was not easily obtained. However, the studies of pure Fe sulfurization suggest an upper limit for the activation energy of 42 kJ mol^{-1} while those of meteoritic metal sulfurization in 50 ppm H_2S yield an upper limit of 50 kJ mol^{-1}. Thus, we use a value of 50 kJ mol^{-1} in our calculations. It is likely that the activation energy for troilite formation is lower than this for the conditions expected in the solar nebula. Thus this activation energy value will yield an upper limit for our estimation for the timescale of troilite formation.

The results of our calculations are shown in Fig. 7. Three different Fe metal grain sizes were considered: 10 nm, 10 μm, and 10 mm. These calculations show that the smallest grains considered will sulfurize well within the estimated cooling time for the solar nebula. Grains that are 10 μm or larger will completely sulfurize at 690 K, but S condensation

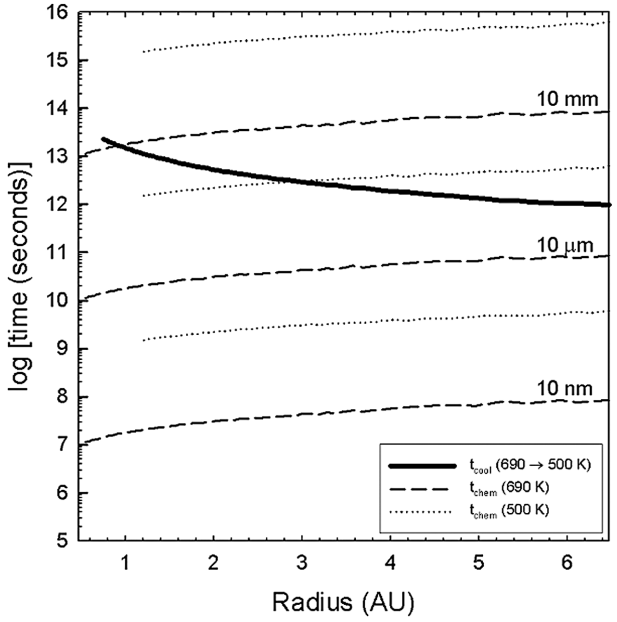

Fig. 7. A graph of the dependence of H_2S–FeS reaction time on metal grain size and radius. The solid line represents the time for the nebula to cool from 690 to 500 K (t_{cool}) and represents our estimate of the amount of time available for S condensation. The dashed lines show the amount of time required to condense 100% of the sulfur in a solar composition system at 690 K while the dotted lines show the same results at 500 K. If $t_{cool} > t_{chem}$, then sulfurization of the metal can proceed. For log time in years, subtract 7.5 from the y-axis.

will be kinetically inhibited at lower temperatures (500 K) in the outer regions of the nebula (> 3 AU). The larger grains (10 mm) will remain relatively unaltered throughout the early history of the solar nebula.

We apply the kinetic considerations determined in this section to a gas diffusion model in an attempt to discern the effect of having a large sulfur sink (in the form of FeS) on the distribution of sulfur in the early solar nebula in the next section. These calculations influence our overall sulfur distribution, especially in the region of planetary formation.

4.3. Sulfur diffusion calculations

As the solar nebula evolved, the molecular species in the gas were redistributed by diffusion (Pringle, 1981). This idea was explored by Stevenson and Lunine (1988) and Cyr et al. (1998) in looking at the distribution of water vapor over time in the nebula. These authors found that the inner nebula would be rapidly depleted in water vapor over a time of $\sim 10^5$ years as water diffused out to the snow line where it condensed forming water ice.

We have applied a model similar to the ones used by Stevenson and Lunine (1988) and Cyr et al. (1998) to study the distribution of the gases H_2S and H_2O in the nebula. H_2S is assumed to be lost in the regions of the nebula where troilite forms. Troilite begins to form at a temperature of $\sim$ 690 K, though its formation may be kinetically inhibited at low temperatures (see Section 4.2). To account for this in our model, we assume that H_2S is removed from the gas phase in regions of the nebula that are between 500 and 690 K. Sunward of this region, troilite does not form because it is still too hot. On the anti-Sun side of this region, the kinetics of the reaction are assumed to be too slow for H_2S to form. At this temperature, 10 μm Fe grains (among the smallest grains observed in meteorites) take roughly 10^5 years to sulfurize, which is comparable to the time it takes for there to be noticeable evolution of the nebula thermal profile. Thus, this temperature is used as a lower limit for the reaction to be completed. Below temperatures of $\sim$ 110 K, $(NH_4)_2S$ is a potential sulfur-bearing condensate (Fegley and Lewis, 1980). At these low temperatures, diffusion occurs very slowly, so if these species are present, they will not affect this diffusion calculation. Compounds related to these species may be in comets. Water vapor is assumed to be lost as it condenses beyond the snow line (temperatures below $\sim$ 160 K) without any kinetic considerations.

To model the distribution of the two species, we use the two-dimensional diffusion equation in cylindrical coordinates assuming azimuthal symmetry following Stevenson and Lunine (1988) and Cyr et al. (1998):

$$\frac{\partial C}{\partial t} = \frac{1}{r}\frac{\partial}{\partial r}\left(r D(r)\frac{\partial C}{\partial r}\right),$$

where C is the relative concentration of the molecular species of interest and $D(r)$ is the diffusion coefficient (note: Stevenson and Lunine (1988) and Cyr et al. (1998) used a diffusion coefficient that did not vary with distance from the Sun). The diffusion coefficient is found using local nebular parameters such that:

$$D(r) = \alpha\frac{c_s^2}{\Omega_K},$$

where α is the viscous turbulence parameter (set to 0.009 to be consistent with the nebula model used here), c_s is the local speed of sound, and Ω_K is the local Keplerian angular velocity. Note that a more detailed calculation would include consideration of the changing surface density with time. Such a consideration is beyond the scope of this paper. Here we attempt to show roughly how the two concentrations change with time.

We apply this model to a snapshot of the nebula at the instant when the water condensation front is at 5 AU. This occurs at a time of 0.44 Ma in the nominal nebula model. The initial conditions of the model are found by taking the nebular profile (pressure and temperature at the midplane as a function of distance from the Sun) and calculating the midplane hydrogen number density assuming an ideal gas. Initially, H_2S and H_2O are assumed to be distributed at the relative solar ratio given by Grevesse and Sauval (1998) and Supulver and Lin (2000). In the regions of the nebula where troilite and water ice are assumed to form, the relative concentrations of the respective species are set to zero. (This is an approximation since Fig. 4A illustrates that the

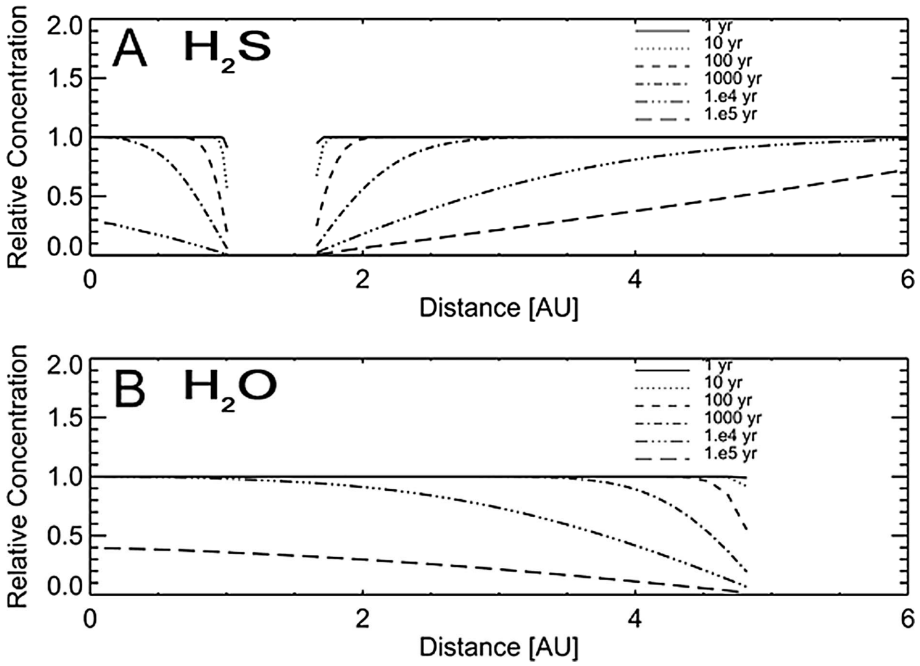

Fig. 8. Graph of the diffusion of both (A) H_2S and (B) H_2O, in the solar nebula, assuming a reaction zone for H_2S from 500–690 K. The times marked represent the amount of time after the starting time of 0.44 Ma. Everything is normalized to its initial local abundance.

H_2S concentration gradually drops to a very low concentration. For our purposes, decreases in the concentrations by an order of magnitude are significant. Note that the axes of the plots in Fig. 8 are linear and not logarithmic.) We also determine Fe grain size limitations based on the reaction kinetics which would be consistent with this initial sulfur distribution. Assuming that all FeS forms in the region between 1 and 1.6 AU, as shown in Fig. 8, the maximum allowable grain size is 10 mm or less near the Sun, and ~ 3 mm out at the edge of the reaction front. This is based on a comparison between the amount of time required for the reaction to occur and the cooling time of the nebula. We note that the local cooling rate in the nebula depends on nebular structure and location, and models generally show that the outer nebula reaches low temperatures more rapidly than the inner nebula (Cassen, 1994; Hersant et al., 2001).

We assume that the temperature structure of the nebula is constant during the time considered and that diffusion is the only method by which any molecular species is transported within the nebula (i.e., there was no migration or decomposition of troilite or water ice, and no significant advective flow of the gas). Lastly, we assume that the troilite formation is not inhibited by iron depletion in the region where it forms.

Figure 8 illustrates how the H_2S and H_2O profiles evolve with time, plotting the concentrations at different radii relative to what they were at the starting time (0.44 Ma) at that radius. Troilite forms between ~ 1.0 and ~ 1.6 AU (Sections 4.1 and 4.2), which is illustrated by the gaps in the profiles on the graph. H_2S diffusion occurs more rapidly than H_2O diffusion due to a larger concentration gradient. Note that the region interior to the gap where troilite forms is quickly depleted in H_2S (in $\sim 10^4$ years), and this occurs before any significant H_2O is lost in that region. Thus, the nebula is too oxidizing to allow significant MgS to form there. If we examine the nebula at a time later in its existence ($\sim 10^5$ years), then regions of low O and S fugacities coexist as a result of diffusion. Our set of condensation calculations with realistic O depletions suggests that the only effect this has on the equilibrium chemistry is a lower condensation temperature of the sulfides MgS and CaS. The condensation temperature of FeS is unaffected.

We also performed similar calculations for nebula profiles when the water ice condensation front reached 4 and 3 AU. In these cooler profiles, the troilite formation zone was between 0.8 and 1.3 AU and 0.6 and 1.0 AU for those respective times. The same general trend was seen in these calculations as in Fig. 8; those regions that rapidly lost H_2S did not lose significant amounts of water vapor on the same timescale. Thus the major sulfide should still be FeS (as noted in Fig. 4). It should be noted that the time for the water ice condensation front to migrate from 5 to 4 AU was 1.9×10^5 years and for it to move from 4 to 3 AU took 3.7×10^5 years. Thus the diffusion profiles shown for 10^5 years may not be valid since we required that the temperature of the nebula not change during the time considered. However, for times of 10^4 years or less (thus the time it takes for the inner nebula to lose its H_2S), it is reasonable to assume that the temperature profile does not change significantly.

If we assume that the profiles shown at 10^5 years are valid, even if the condensation front has migrated sunwards by some fraction of an AU, then there exist regions of depleted O concentrations. Such regions correspond to C/O

values greater than 0.5. In these regions, a dual sink situation may be active, wherein both MgS and FeS form, removing H_2S (g) from the system. More detailed calculations of such a system would depend on the kinetics of the formation of MgS, which are unknown.

5. Discussion

We have calculated the equilibrium condensation chemistry of sulfur coupled with the diffusion of water and sulfur in the nebula and with kinetic considerations for the dominant solid sulfide phase, troilite. We find that a solar-composition nebula is too oxidizing to form the reduced condensed sulfur-bearing species MgS and CaS in significant amounts, consistent with meteoritic observations. We also demonstrate that the gas H_2S is still present at temperatures lower than 500 K, due to the slow reaction kinetics for the formation of troilite at these temperatures. We find that by varying oxygen fugacity, the major sulfur-bearing gas species changes from H_2S at high O abundance to SiS at low O abundance. In addition, we find FeS to be the dominant S-bearing solid species at high oxygen fugacities, whereas MgS, CaS, and FeS are the major sulfide species at lower oxygen fugacities. We apply our results in a qualitative fashion to meteorites, Jupiter, and observations of protoplanetary disks beyond our own Solar System.

5.1. Applications to meteorites

The majority of meteorites are members of the ordinary chondrite class. These meteorites contain abundant magnesium silicates, iron metal, and FeS. The observed modal FeS to iron metal ratio is usually significantly less than 1, implying incomplete reaction of iron and sulfur. Our results are consistent with this, since the kinetics in Section 4.2 suggest that there would not be time for the complete conversion of iron metal to troilite. FeS is by far the most common sulfur bearing mineral in primitive meteorites. However, the enstatite chondrites also possess several accessory sulfide minerals. Enstatite chondrites are a peculiar meteorite class whose mineralogy is dominated by enstatite ($MgSiO_3$) and which display evidence of formation in a very reducing environment. Enstatite chondrites are grouped into two classes: the EH chondrites are enstatite chondrites with high total iron content, and the EL chondrites are those with low iron content. EH chondrites contain MgS, whereas EL chondrites contain the more ferroan alabandite, (Mn,Fe)S (Ehlers and El Goresy, 1988). Enstatite chondrites also contain oldhamite (CaS) and silicon dissolved in iron metal. Very few other meteorite classes contain these compounds, and as a result, they have been the subject of much study in an attempt to determine their origin.

Many different studies have been performed to see if it is possible to replicate the observed mineralogy of enstatite chondrites using condensation calculations. Larimer (1968) studied the presence and significance of oldhamite in meteorites and was among the first to suggest that in order to reproduce the observed mineralogy of enstatite chondrites, nebular heterogeneities were required. He suggested that a slight C/O fractionation may have occurred in certain regions of the solar nebula. Baedecker and Wasson (1975) outlined several potential mechanisms for the formation of enstatite chondrites, the first of which was the depletion of an oxidizing agent (like water) from the solar nebula. Herndon and Suess (1976) attempted to show that enstatite chondrite minerals could form in a solar nebula with pressures of approximately 1 bar. Larimer and Bartholomay (1979) addressed this proposed mechanism, finding that Herndon and Suess (1976) had omitted several important high temperature silicate condensates, and that these would form instead of the more reduced minerals suggested by Herndon and Suess (1976). Most recently, Hutson and Ruzicka (2000) replicated the mineralogy of enstatite chondrites by coupling the water depletion of Cyr et al. (1998) with a depletion of refractory components. This work supports Hutson and Ruzicka (2000), agreeing with their suggestion that some of the minerals in enstatite chondrites formed through the heterogeneities resulting from the ice condensation front. According to our models, we suggest that between 50–70% of the oxygen was removed by diffusion to form these accessory sulfide minerals. We also calculate that the timescale for the formation of the these minerals is approximately 10^5 years or more, based on the results portrayed in Fig. 8. The location of the formation of enstatite chondrites is more difficult to constrain with our model, but it must have been beyond the troilite condensation front, but before the water ice condensation front (as enstatite chondrites have no recorded aqueous alteration products). Thus we predict that the enstatite chondrites formed between ~ 1 and ~ 4 AU. This model does not explain all of the minerals or phases in enstatite chondrites (like CAIs or chondrules), but it provides an explanation for the sulfide phases consistent with the overall reduced character of these meteorites.

5.2. Applications to Jupiter

The abundance of elemental sulfur in Jupiter measured by the Galileo probe is approximately three times solar, in rough agreement with the noble gases and carbon- and nitrogen-bearing species (Atreya et al., 2003). One interpretation of this pattern is that it is a direct reflection of the abundance pattern in very cold planetesimals that entered Jupiter with little alteration from the molecular cloud (Owen et al., 1999). An alternative model is that planetesimals formed locally in the region of Jupiter, cooling slowly and accommodating volatiles by trapping them in the ice as clathrate hydrates (Gautier et al., 2001). This last model predicts an overabundance of sulfur in Jupiter, introduced as hydrogen sulfide, by a factor of two over what is observed. One possible way to reconcile this model with the Galileo measurements is to postulate a depletion of H_2S

in the region near Jupiter where planetesimals formed and then were accreted onto the giant planet. Our results suggest that such a depletion is possible as a result of the coupling between the oxygen-dependent sulfur chemistry, the FeS kinetics, and the nebular transport processes that affect both the water (hence oxygen) abundance via cold trapping and the sulfur abundance at and beyond the FeS boundary. More detailed numerical transport models are required to test this assertion and can be put on a firm footing using the thermochemical results and approximate kinetic considerations given here. Meanwhile, the two models for the origin of the heavy element enrichment in Jupiter can be definitively tested only with future missions that will measure the deep oxygen abundance of Jupiter (Lunine et al., 2003).

5.3. Disks

The results of our calculations have important implications for future observations of molecular species in protoplanetary accretion disks surrounding low mass stars. Because sulfur is the most volatile of all the major rock-forming elements, it is likely to remain in the gas-phase for longer times and out to larger radii than the other abundant elements such as Mg, Fe, and Si.

An important transition in the distribution of sulfur-bearing species inward of 5 AU (Fig. 6) occurs when the inner nebula is depleted in oxygen by 30%. The most abundant gaseous species changes from H_2S to SiS. Both of these molecules are observable using current astronomical facilities. Furthermore, future sub-mm interferometers such as ALMA will be capable of measuring chemical composition gradients in the inner regions of nearby protoplanetary accretion disks. Thus, determination of the H_2S/SiS ratio in these objects can provide evidence for the presence of a nebular snow line and can constrain the oxidation state and major element chemistry in the inner regions, where rocky planets are likely to form.

Acknowledgments

We thank Franck Hersant for providing us with the nebular model. We also thank Alex Ruzicka and Michail Petaev for many helpful comments in review. This work was supported by NASA grants NAG5-11355 (DSL) and NAG5-10450 (JIL).

Appendix A.1
Gaseous species: first column is SOLGASMIX code, second is HSC5

Al	Al	–	F_2	NaH	NaH
Al_2O	Al_2O	Fe	Fe	NaO	NaO
Al_2S	Al_2S	FeH	–	NaOH	NaOH
AlH	AlH	FeO	–	Ne	Ne
AlO	AlO	FeS	–	Ni	Ni
AlO_2	AlO_2	H	H	$Ni(CO)_4$	–
AlOH	AlOH	H_2	H_2	NiCl	–
AlS	AlS	H_2O	H_2O	$NiCl_2$	–
AlS_2	AlS_2	H_2SO_4	H_2SO_4	NiH	–
Ar	C	H_2S	H_2S	NiO	–
C	C_2H_2	HCl	HCl	NiS	NiS
C_2H_2	C_2H_4	HCN	HCN	O	–
C_2H_4	C_2H_6	HCNO	–	O_2	O_2
C_2H_4O	C_3H_8	HCO	HCO	OH	OH
C_4N_2	C_4N_2	–	HF	P	P
CCl_2	CCl_2	HNO	HNO	–	P_2
CH	CH	HOCl	HOCl	P_4O_6	P_4O_6
CH_2	CH_2	HS	HS	PH	PH
CH_2O	CH_2O	He	He	PH_2	PH_2
CH_3	CH_3	K	K	PH_3	PH_3
CH_4	CH_4	K_2SO_4	–	PN	PN
CN	CN	KCl	KCl	PO	PO
CO	CO	KCN	KCN	PS	PS
CO_2	CO_2	KH	KH	S	S
COS	COS	KOH	KOH	S_2	S_2
CP	CP	Mg	Mg	S_2O	S_2O
CS	CS	MgH	MgH	SN	SN
CS_2	CS_2	MgS	MgS	SO	SO
Ca	Ca	MnH	–	SO_2	SO_2
CaH	CaH	MnO	–	Si	Si
CaOH	CaOH	MnS	–	SiC	SiC
CaS	CaS	N	–	SiH	SiH
Cl	Cl	N_2	N_2	–	SiH_2
Cl_2	Cl_2	N_2H_2	N_2H_2	–	SiH_4
ClO	ClO	N_2O	N_2O	–	SiN
Co	–	NCO	–	SiO	SiO
CoCl	–	NH	NH	SiS	SiS
$CoCl_2$	–	NH_2	NH_2	Ti	Ti
$CoCl_3$	–	NH_3	NH_3	TiC_2	–
Cr	Cr	NO	NO	TiC_4	–
CrC_2	–	NO_2	NO_2	TiCl	TiCl
CrH	CrH	Na	Na	$TiCl_2$	$TiCl_2$
CrN	CrN	Na_2Cl_2	–	TiH	–
CrO	CrO	$Na_2O_2H_2$	–	TiN	TiN
CrO_2	CrO_2	Na_2SO_4	–	TiO	TiO
CrO_3	CrO_3	NaCl	NaCl	TiO_2	TiO_2
–	F	NaCN	NaCN	TiS	TiS

– is not included.

Appendix A.2
Solid species: first column is SOLGASMIX code, second is HSC5

Al_2O_3	Al_2O_3	–	Fe_3Si	–	SiS_2
–	Al_2S_3	–	FeSi	Ti	Ti
Al_2SiO_5	–	–	$FeSi_2$	Ti_2O_3	–
$Al_6Si_2O_{13}$	–	$Fe_2(SO_4)_3$	–	Ti_3O_5	–
AlN	AlN	Fe_2SiO_4	Fe_2SiO_4	Ti_4O_7	Ti_4O_7
C	C	$FeSiO_3$	$FeSiO_3$	TiC	TiC
$Ca_2Al_2SiO_7$	$Ca_2Al_2SiO_7$	$FeSO_4$	–	$TiCl_2$	–
$Ca_2MgSi_2O_7$	$Ca_2MgSi_2O_7$	–	$FeTiO_3$	TiN	TiN
$Ca_3(PO_4)_2$	$Ca_3(PO_4)_2$	–	H_2O	TiO	–
$Ca_3Ti_2O_7$	–	K_2S	K_2S	TiO_2	–
$Ca_4Ti_3O_{10}$	$Ca_4Ti_3O_{10}$	K_2SO_4	–		
–	$Ca_5(PO_4)_3F$	$KAlSi_3O_8$	$KAlSi_3O_8$		
–	$Ca_5(PO_4)_3OH$	KCl	KCl		
$CaAl_{12}O_{19}$	$CaAl_{12}O_{19}$	Mg_2SiO_4	Mg_2SiO_4		
$CaAl_2O_4$	$CaAl_2O_4$	Mg_2TiO_4	–		
$CaAl_2Si_2O_8$	$CaAl_2Si_2O_8$	$Mg_3(PO_4)_2$	–		
–	$CaAl_2SiO_6$	$MgAl_2O_4$	$MgAl_2O_4$		
–	$CaFe(SiO_3)_2$	MgS	MgS		
$CaMgSi_2O_6$	$CaMgSi_2O_6$	$MgSiO_3$	$MgSiO_3$		
CaO	–	$MgSO_4$	–		
CaS	CaS	$MgTi_2O_5$	–		

(*continued on next page*)

Appendix A.2 (*continued*)

$CaSiO_3$	$CaSiO_3$	$MgTiO_3$	–
$CaSO_4$	–	Mn	–
$CaTiO_3$	$CaTiO_3$	Mn_2SiO_4	–
Co	–	MnO	–
Co_3O_4	–	$MnSiO_3$	–
$CoCl_2$	–	–	$(NH_4)_2S$
CoO	–	Na_2S	Na_2S
$CoSO_4$	–	Na_2SiO_3	Na_2SiO_3
Cr	Cr	Na_2SO_4	–
Cr_2N	–	$NaAlSi_3O_8$	$NaAlSi_3O_8$
Cr_2O_3	Cr_2O_3	NaCl	NaCl
CrN	CrN	$(NH_4)_2SO_4$	–
CrO_2	CrO_2	Ni	Ni
CrS	CrS	Ni_3S_2	–
Fe	Fe	Ni_3S_4	–
Fe_3C	Fe_3C	$NiCl_2$	–
$FeCr_2O_4$	$FeCr_2O_4$	$NiCr_2O_4$	–
$FeCr_2S_4$	–	NiS	NiS
FeO	–	NiS_2	–
–	$Fe_{0.947}O$	–	P
Fe_3O_4	Fe_3O_4	P_4O_{10}	–
–	Fe_2O_3	Si_3N_4	–
Fe_3P	Fe_3P	–	Si_2N_2O
FeS	FeS	SiC	SiC
–	FeS_2	–	SiS

– is not included.

References

Atreya, S.K., Mahaffy, P., Niemann, H.B., Wong, M.H., Owen, T., 2003. Comparison of the atmospheres of Jupiter and Saturn: deep atmospheric composition, cloud structure, vertical mixing, and origin. Planet. Space Sci. 47, 1243–1262.

Baedecker, P.A., Wasson, J.T., 1975. Elemental fractionations among enstatite chondrites. Geochim. Cosmochim. Acta 39, 735–765.

Barin, I., 1995. Thermochemical Data of Pure Substances. VCH Publishers, Weinheim, Germany.

Bessman, T.M., 1977. SOLGASMIX-PV—a computer program to calculate equilibrium relationships in complex chemical systems. Oak Ridge National Laboratory Rep. TM-5775, ORNL, Oak Ridge.

Bockelée-Morvan, D., Gautier, D., Hersant, F., Huré, J.-M., Robert, F., 2002. Turbulent radial mixing in the solar nebula as the source of crystalline silicates in comets. Astron. Astrophys. 384, 1107–1118.

Burrows, A., Sharp, C.M., 1999. Chemical equilibrium abundances in brown dwarfs and extrasolar giant planet atmospheres. Astrophys. J. 512, 843–863.

Cassen, P., 1994. Utilitarian models of the solar nebula. Icarus 112, 405–429.

Cassen, P., 2001. Nebular thermal evolution and the properties of primitive planetary materials. Meteorit. Planet. Sci. 36, 671–700.

Chase, M.W., 1982. JANAF Thermodynamic Tables, Magnetic Tape Version. Dow Chemical Company, Midland.

Chase, M.W., 1998. NIST-JANAF thermochemical tables, fourth ed. J. Phys. Chem. Ref. Data Monogr. 9.

Cyr, K.E., Sears, W.D., Lunine, J.I., 1998. Distribution and evolution of water ice in the solar nebula: implications for Solar System body formation. Icarus 135, 537–548.

Cyr, K.E., Sharp, C.M., Lunine, J.I., 1999. Effects of the redistribution of water in the solar nebula on nebular chemistry. J. Geophys. Res. 104, 19003–19014.

Drouart, A., Dubrulle, B., Gautier, D., Robert, F., 1999. Structure and transport in the solar nebula from constraints on deuterium enrichment and giant planets formation. Icarus 140, 129–155.

Dulick, M., Bauschlicher Jr., C.W., Burrows, A., Sharp, C.M., Ram, R.S., Bernath, P., Line intensities and molecular opacities of the FeH $F^4\Delta_i$–$X^4\Delta_i$ transition. Astrophys. J. In press.

Dutrey, R.M., Guilloteau, S., Guelin, M., 1997. Chemistry of protosolar-like nebulae: the molecular content of the DM Tau and GG Tau disks. Astron. Astrophys. 317, L55–L58.

Ehlers, K., El Goresy, A., 1988. Normal and reverse zoning in niningerite: a novel key parameter to the thermal histories of EH chondrites. Geochim. Cosmochim. Acta 52, 877–887.

Eriksson, G., Rosen, E., 1973. Thermodynamic studies of high-temperature equilibria. 8. General equation for calculation of equilibria in multiphase systems. Chem. Scripta 4, 193–194.

Fegley Jr., B., 1988. Cosmochemical trends of volatile elements in the Solar System. In: Nuth, J.A., Sylvester, P.J. (Eds.), Workshop on the Origins of Solar Systems, pp. 51–60. LPI Technical Report No. 88-04.

Fegley, B., Lewis, J.S., 1980. Volatile element chemistry in the solar nebula: Na, K, F, Cl, Br, and P. Icarus 41, 439–455.

Gautier, D., Hersant, F., Mousis, O., Lunine, J.I., 2001. Enrichments in volatiles in Jupiter: a new interpretation of the Galileo measurements. Astrophys. J. 550, L227–L230. Erratum: Astrophys. J. 559 (2001) L183.

Grevesse, N., Sauval, A.J., 1998. Standard solar composition. Space Sci. Rev. 85, 161–174.

Gurvich, L.V., Veyts, I.V., Alcock, C.B., 1994. Thermodynamic Properties of Individual Substances, vol. 3, fourth ed. Hemisphere Publishing, New York.

Hallstedt, B., 1990. Assessment of the CaO–Al_2O_3 system. J. Am. Ceramics Soc. 73, 15–23.

Hartmann, L., Calvet, N., Gullbring, E., D'Alessio, P., 1998. Accretion and the evolution of T Tauri disks. Astrophys. J. 495, 385–400.

Herndon, J.M., Suess, H.E., 1976. Can enstatite meteorites form from a nebula of solar composition? Geochim. Cosmochim. Acta 40, 395–399.

Hersant, F., Gautier, D., Huré, J., 2001. A two-dimensional model for the primordial nebula constrained by D/H measurements in the Solar System: implications for the formation of giant planets. Astrophys. J. 554, 391–407.

Huré, J.-M., 2000. On the transition to self-gravity in low mass AGN and YSO accretion discs. Astron. Astrophys. 358, 378–394.

Hutson, M.A., Ruzicka, A., 2000. A multi-step model for the origin of E3 (enstatite) chondrites. Meteorit. Planet. Sci. 35, 601–608.

Kassel, L.S., 1933a. Thermodynamic calculations from spectral data. Phys. Rev. 43, 364–365.

Kassel, L.S., 1933b. Mathematical methods for computing thermodynamic functions from spectral data. J. Chem. Phys. 1, 576–585.

Knacke, O., Kubaschewski, O., Hesselmann, K., 1991. Thermochemical Properties of Inorganic Substances. Springer-Verlag, Heidelberg.

Larimer, J.W., 1968. An experimental investigation of oldhamite CaS and the petrologic significance of oldhamite in meteorites. Geochim. Cosmochim. Acta 32, 965–982.

Larimer, J.W., Bartholomay, M., 1979. The role of carbon and oxygen in cosmic gases: some applications to the chemistry and mineralogy of enstatite chondrites. Geochim. Cosmochim. Acta 43, 1455–1466.

Lauretta, D.S., Kremser, D.T., Fegley, B.J., 1996. The rate of iron sulfide formation in the solar nebula. Icarus 122, 288–315.

Lauretta, D.S., Lodders, K., Fegley, B., 1997. Experimental simulations of sulfide formation in the solar nebula. Science 277, 358–360.

Lauretta, D.S., Lodders, K., Fegley, B., 1998. Kamacite sulfurization in the solar nebula. Meteorit. Planet. Sci. 33, 821–833.

Lodders, K., 1999. Revised thermochemical properties of phosphinidene (PH), phosphine (PH_3), phosphorus nitride (PN), and magnesium phosphate ($Mg_3P_2O_8$). J. Phys. Chem. Ref. Data 28, 1705–1712.

Lodders, K., 2003. Solar System abundances and condensation temperatures of the elements. Astrophys. J. 591, 1220–1247.

Lunine, J.I., Owen, T.C., Brown, R.H., 2000. The outer Solar System: chemical constraints at low temperatures on planet formation. In: Mannings, V., Boss, A.P., Russel, S. (Eds.), Protostars and Planets IV. Univ. of Arizona Press, Tucson, pp. 1055–1080.

Lunine, J.I., Coradini, A., Gautier, D., Owen, T., Wuchterl, G., 2003. The origin of Jupiter. In: Bagenal, F. (Ed.), Jupiter. Cambridge Univ. Press, London. In press.

Makalkin, A.B., Dorofeyeva, V.A., 1991. Temperatures in the protoplanetary disk: models, constraints and consequences for the planets. Izv. Earth Phys. 27, 650–664.

Morfill, G.E., Volk, H.J., 1984. Transport of dust and vapor and chemical fractionation in the early protosolar cloud. Astrophys. J. 287, 371–395.

Owen, T., Mahaffy, P., Niemann, H.B., Atreya, S.K., Donahue, T.M., Bar-Nun, A., de Pater, I., 1999. A new constraint on the formation of giant planets. Nature 402, 269–270.

Petaev, M.I., Lavrukhina, A.K., Khodakovskiy, I.L., 1986. Genesis of minerals of enstatite meteorites. Geokhimiya 9, 1219–1232.

Prieto, C.A., Lambert, D.L., Asplund, M., 2001. The forbidden abundance of oxygen in the Sun. Astrophys. J. 556, L63–L66.

Prieto, C.A., Lambert, D.L., Asplund, M., 2002. A reappraisal of the solar photospheric C/O ratio. Astrophys. J. 573, L137–L140.

Pringle, J.E., 1981. Accretion discs in astrophysics. Annu. Rev. Astron. Astrophys. 19, 137–162.

Salpeter, E.E., 1974. Nucleation and growth of dust grains. Astrophys. J. 193, 579–584.

Shakura, N.I., Sunyaev, R.A., 1973. Black holes in binary systems. Observational appearance. Astron. Astrophys. 24, 337–355.

Sharp, C.M., Huebner, W.F., 1990. Molecular equilibrium with condensation. Astrophys. J. Suppl. Ser. 72, 417–431.

Sharp, C.M., Huebner, W.F., 1993. Molecular equations of state with condensation (MESC) for astrophysical applications. Southwest Research Institute Report 93-1.

Shu, F.H., Tremaine, S., Adams, F.C., Ruden, S.P., 1990. Sling amplification and eccentric gravitational instabilities in gaseous disks. Astrophys. J. 358, 495–514.

Stevenson, D.J., Lunine, J.I., 1988. Rapid formation of Jupiter by diffuse redistribution of water vapor in the solar nebula. Icarus 75, 146–155.

Supulver, K.D., Lin, D.N.C., 2000. Formation of icy planetesimals in a turbulent solar nebula. Icarus 146, 525–540.

Weck, P.F., Schweitzer, A., Stancil, P.C., Hauschildt, P.H., Kirby, K., 2003. The molecular line opacity of MgH in cool stellar atmospheres. Astrophys. J. 582, 1059–1065.

White, W.B., Johnson, S.M., Dantzig, G.B., 1958. Chemical equilibrium in complex mixtures. J. Chem. Phys. 28, 751–755.

Wood, J.A., Hashimoto, A., 1993. Mineral equilibrium in fractionated nebular systems. Geochim. Cosmochim. Acta 57, 2377–2388.

Zaitsev, A.I., Dobrokhotova, Z.V., Litvina, A.D., Mogutnov, B.M., 1995. Thermodynamic properties and phase equilibria in the Fe–P system. J. Chem. Soc. Faraday Trans. 91, 703–712.